inorganics

MDPI

Article

Hydrogen Sorption in Erbium Borohydride Composite Mixtures with $LiBH_4$ and/or LiH

Michael Heere [1], Seyed Hosein Payandeh GharibDoust [2], Matteo Brighi [3], Christoph Frommen [1], Magnus H. Sørby [1], Radovan Černý [3], Torben R. Jensen [2] and Bjørn C. Hauback [1,*]

1 Physics Department, Institute for Energy Technology, NO-2027 Kjeller, Norway; heere.michael@gmail.com (M.H.); Christoph.Frommen@ife.no (C.F.); Magnus.Sorby@ife.no (M.H.S.)
2 Interdisciplinary Nanoscience Center (iNANO) and Department of Chemistry, University of Århus, Langelandsgade 140, DK-8000 Århus C, Denmark; hosein.payandeh@inano.au.dk (S.H.P.G.); trj@chem.au.dk (T.R.J.)
3 Laboratory of Crystallography, Department of Quantum Matter Physics, University of Geneva, Quai Ernest-Ansermet 24, Ch-1211 Geneva, Switzerland; Matteo.Brighi@unige.ch (M.B.); Radovan.Cerny@unige.ch (R.Č.)
* Correspondence: Bjorn.Hauback@ife.no; Tel.: +47-9740-8844

Academic Editor: Hiroshi Kageyama
Received: 27 March 2017; Accepted: 20 April 2017; Published: 26 April 2017

Abstract: Rare earth (RE) metal borohydrides have recently been receiving attention as possible hydrogen storage materials and solid-state Li-ion conductors. In this paper, the decomposition and reabsorption of $Er(BH_4)_3$ in composite mixtures with $LiBH_4$ and/or LiH were investigated. The composite of $3LiBH_4$ + $Er(BH_4)_3$ + 3LiH has a theoretical hydrogen storage capacity of 9 wt %, nevertheless, only 6 wt % hydrogen are accessible due to the formation of thermally stable LiH. Hydrogen sorption measurements in a Sieverts-type apparatus revealed that during three desorption-absorption cycles of $3LiBH_4$ + $Er(BH_4)_3$ + 3LiH, the composite desorbed 4.2, 3.7 and 3.5 wt % H for the first, second and third cycle, respectively, and thus showed good rehydrogenation behavior. In situ synchrotron radiation powder X-ray diffraction (SR-PXD) after ball milling of $Er(BH_4)_3$ + 6LiH resulted in the formation of $LiBH_4$, revealing that metathesis reactions occurred during milling in these systems. Impedance spectroscopy of absorbed $Er(BH_4)_3$ + 6LiH showed an exceptional high hysteresis of 40–60 K for the transition between the high and low temperature phases of $LiBH_4$, indicating that the high temperature phase of $LiBH_4$ is stabilized in the composite.

Keywords: borohydride; rare earth element; hydrogen storage; decomposition; solid state electrolyte

1. Introduction

One of the most promising candidates for solid state hydrogen storage applications is $LiBH_4$, which has a theoretical capacity of 18.5 wt % H_2. The practical hydrogen amount that can be desorbed is 13.8 wt %, due to the formation of very stable LiH during decomposition, but $LiBH_4$ is still among the materials with the highest hydrogen capacity considered for solid state storage [1,2]. However, it requires very tough conditions for rehydrogenation [3] and suffers from capacity loss on cycling due to the formation of higher boranes [4]. Another class of materials to be considered is rare earth (RE) borohydrides, with hydrogen capacities varying between 9.0 wt % for $Y(BH_4)_3$ and 5.5 wt % for $Yb(BH_4)_3$ [5–19]. Li-containing RE borohydrides are also considered as solid state electrolytes for new battery applications, due to their high Li-ion conductivities [20–23]. RE borohydrides have shown novel properties such as luminescence, and a magnetocaloric effect has also been recently published [24–26].

Gennari et al. investigated the composite mixtures of $6LiBH_4$ and $RECl_3$ with RE = Ce, Gd and found a decrease in decomposition temperature of $LiBH_4$ due to an in situ formed REH_2 phase [17]. Additionally, the decomposed composite showed the ability to reabsorb 20% of the initial hydrogen content. Frommen et al. investigated the composite mixtures of $LiBH_4$, LiH and $RE(BH_4)_3$ with RE = La, Er [27]. It was reported that the desorption temperature of $LiBH_4$ in the mixture with RE = Er decreased by about 100 °C compared to pure $LiBH_4$. Reabsorption at 340 °C under 100 bar H_2 yielded a hydrogen uptake of 66% after desorption against vacuum, and 80% after desorption against 5 bar H_2, respectively, of the initially release of 3 wt % H_2.

The established technique to synthesize RE borohydrides is the solid state metathesis approach, as it has the advantage of direct synthesis of a RE borohydride without complicated in vacuo manipulations or possible decomposition [28,29]. The RE chloride and an alkali metal borohydride (i.e., Li, Na, K) are mixed in a one-step mechanochemical synthesis to form the RE borohydride and the alkali metal chloride via a metathesis reaction. $LiBH_4$ has proven to be an efficient precursor, but also other metal borohydrides e.g., $NaBH_4$, have been successfully used [30–32]. As an alternative method, the solvent-based synthesis of borohydrides has been used for over 50 years with the advantage of removing the alkali metal chloride (i.e., LiCl) [28], which is necessary to increase the hydrogen capacity. The halide-free synthesis in this paper is based on a mechanochemical synthesis [33] and wet-chemical extraction, as described by Hagemann et al. [34,35].

This work presents two new composite materials: $Er(BH_4)_3 + 6LiH$ and $3LiBH_4 + Er(BH_4)_3 + 3LiH$. The decomposition and reabsorption of hydrogen have been studied in detail by in situ synchrotron radiation powder X-ray diffraction (SR-PXD). Desorption-absorption cycling measurements were conducted in a Sieverts-type apparatus. The rehydrogenation properties of the $3LiBH_4 + Er(BH_4)_3 + 3LiH$ system were investigated during three desorption-absorption cycles. One cycle was studied for the $Er(BH_4)_3 + 6LiH$ system. The latter was also investigated by impedance spectroscopy. Finally, thermal gravimetric (TG) and differential scanning calorimetry (DSC), as well as mass spectrometry (MS) were conducted.

2. Results & Discussion

2.1. $Er(BH_4)_3 + 6LiH$ (S1)

Figure 1 shows the in situ synchrotron radiation powder X-ray diffraction (SR-PXD) data of $Er(BH_4)_3 + 6LiH$ (S1) from room temperature (RT) to 280 °C. At RT, Bragg peaks corresponding to LiH, orthorhombic-$LiBH_4$ (o-$LiBH_4$) and ErH_2, as well as minor peaks from $Er(BH_4)_3$, are present, suggesting the reaction pathway of Equation (1) for the ball milling reaction.

$$Er(BH_4)_3(s) + 3LiH(s) \xrightarrow{ball\ milling} ErH_2(s) + 3LiBH_4(s) + 0.5H_2(g) \quad (1)$$

The small amount of $Er(BH_4)_3$ present (Table 1) indicates that Equation (1) has almost gone to completion during milling. The in situ SR-PXD data show the phase transition of o- to hexagonal-$LiBH_4$ (h-$LiBH_4$) at 100 °C. The Bragg peaks of $Er(BH_4)_3$ start to decrease simultaneously and are gone at 240 °C. ErH_2 is present in significant amounts (44.1(4) wt %) directly after ball milling. Its lattice parameters increase more than expected from the thermal expansion from 186 °C, indicating that it is further hydrogenated, induced by the hydrogen pressure in the in situ SR-PXD measurements setup, with a likely intermediate state of $ErH_{2+\delta}$ with ($0 \leq \delta \leq 1$) as shown in Figure S1. Bragg peaks from $LiBH_4$ disappear at 270 °C, caused by its melting. Above 280 °C, the sample oxidizes, as evident from strong Bragg peaks of Er_2O_3 (not shown), and further analysis of the decomposition process was therefore not possible.

Figure 2a shows the differential scanning calorimetry (DSC) data of S1. The phase transition from o- to h-$LiBH_4$ occurs at 105 °C and its melting at 260 °C (peak temperatures), which is in good agreement with the SR-PXD data. A rather minor exothermic DSC event (dashed circle in Figure 2a)

can be seen in analogy to the increase in the lattice parameter observed in SR-PXD starting at 186 °C, corresponding to the reaction from ErH_2 towards ErH_3. The decomposition of the Li borohydride appears at 326 °C. There is a minor endothermic peak after the major endothermic event, which can be assigned to desorption of ErH_3 to ErH_2 (a similar decomposition temperature is observed for pure ErH_3, as shown in Figure S2). Thermogravimetric (TG) data for S1 are also presented in Figure 2 and show mass loss of 3.4 wt % between RT and 400 °C, including a 30-min isotherm.

The powder X-ray diffraction (PXD) pattern of one complete desorption absorption cycle in the Sieverts apparatus is shown in Figure 2b. The main product after desorption at 400 °C and 5–10 bar H_2 is ErH_3, formed by additional hydrogen absorption by ErH_2 upon cooling. Minor Bragg peaks of ErB_4 are also observed. Reabsorption at 340 °C under 100 bar H_2 for 12 h resulted in the formation of $LiBH_4$, as well as increased intensity of ErH_3 peaks.

Table 1. Compositions and synthesis method of the investigated samples. The products after ball milling are given with lattice parameters and fractions from Rietveld refinements of diffraction data at room temperature (RT). Refinements are shown in Table S1. Sample S2 was stored in a glove box for nine months before measurements were taken. Estimated standard deviations are given in parentheses.

Sample	Reactants	Method	Products	Lattice Parameters (Å)	Refined Fractions (wt %)
S1	$Er(BH_4)_3$ + 6LiH	1 h ball milling	$Er(BH_4)_3$	a = 10.884(3)	1.1(2)
			$LiBH_4$	a = 7.174(7) b = 4.426(5) c = 6.807(9)	29.9(3)
			LiH	a = 4.0851(6)	24.8(2)
			ErH_2	a = 5.1458(4)	44.1(4)
S2	$Er(BH_4)_3$ + 3$LiBH_4$ + 3LiH	1 h ball milling	$Er(BH_4)_3$	a = 10.8134(3)	29.7(1)
			$LiBH_4$	a = 7.172(5) b = 4.430(3) c = 6.804(6)	38.2(16)
			LiH	a = 4.0851	0.0(9)
			ErH_2	a = 5.1823(3)	32.1(1)

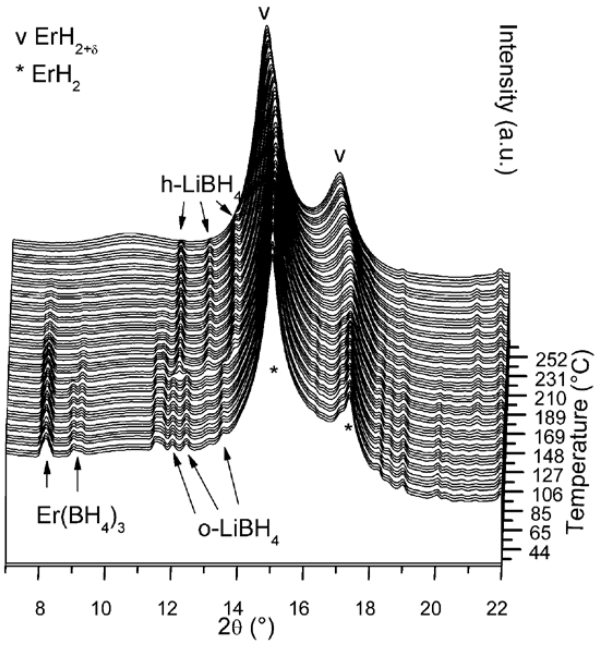

Figure 1. In situ SR-PXD data of sample S1 during heating from RT to 280 °C (5 °C·min^{-1}) under 1 bar H_2. Arrows mark the Bragg peaks of $Er(BH_4)_3$, o- and h-$LiBH_4$. λ = 0.77787 Å.

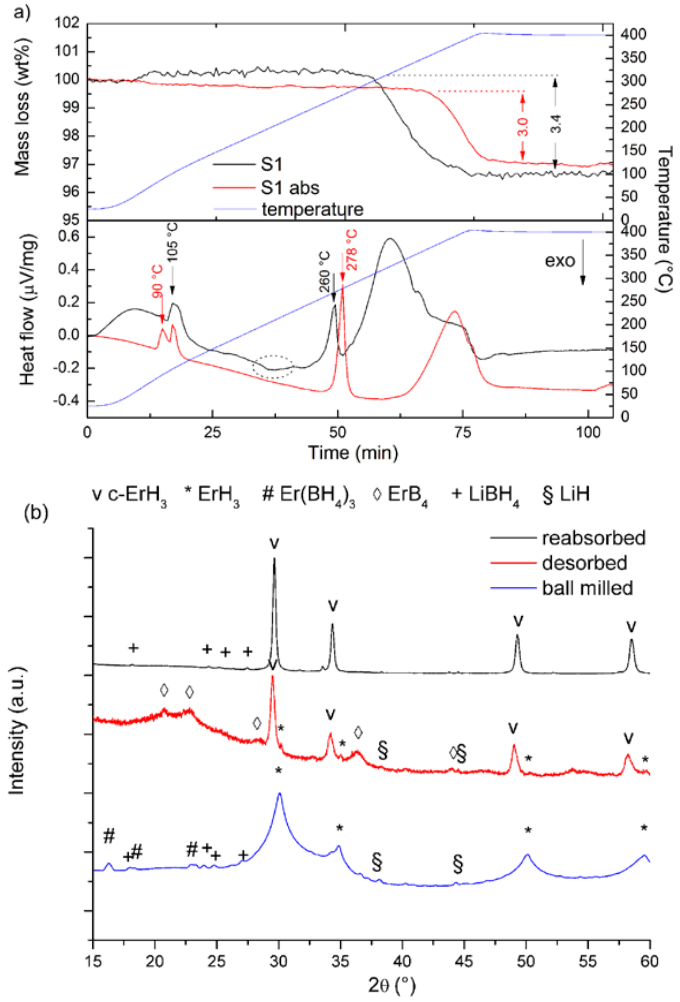

Figure 2. (**a**) TG-DSC data of ball milled S1 (black curves) and reabsorbed S1 (S1 abs) (red curves), showing TG data (top) and DSC signal (bottom). *X*-axis in time (min) as the heating from RT to 400 °C proceeded with a 30-min isotherm. Temperature (°C) is given on the secondary *y*-axis to the right; (**b**) Ex situ PXD data of S1 showing one absorption-desorption cycle with ball milled (bottom), desorbed (middle), and reabsorbed (top) composite. λ = 1.54056 Å.

The thermogravimetric and differential scanning calorimetry (TG-DSC) data for the decomposition of reabsorbed S1 is shown in Figure 2a (red curves). TG data show a mass loss of 3.0 wt %, corresponding to 88% of the initial released hydrogen. An increase in onset temperature of hydrogen release can be observed (ΔT = 70 °C). In the DSC data, two peaks occur at rather low temperatures. The first peak is at 90 °C, but the process behind it is not completely understood (see Li-ion conductivity section). The second one at 105 °C corresponds to the *o*- to h-$LiBH_4$ transition. The melting of $LiBH_4$ occurs at 278 °C. The last endothermic event coincides with the mass loss and occurs at 390 °C, which is probably a superposition of two events. The first is proposed to be the decomposition of $LiBH_4$, while the second is possibly the reduction of ErH_3 to ErH_2, see Figure S2.

In general, the desorption-absorption cycle shown in this section follows the reaction pathways outlined in Equations (2) and (3).

$$4LiBH_4(s) + ErH_2(s) \xrightarrow{desorption} ErB_4(s) + 4LiH(s) + 7H_2(g) \quad (2)$$

$$ErB_4(s) + 4LiH(s) + 7.5H_2(g) \xrightarrow{absorption} 4LiBH_4(s) + ErH_3(s) \quad (3)$$

2.2. $3LiBH_4 + Er(BH_4)_3 + 3LiH$ (S2)

Figure 3a shows the ex situ lab PXD patterns of $3LiBH_4 + Er(BH_4)_3 + 3LiH$ (S2) in the as-milled, desorbed, and reabsorbed states. The Bragg peaks of the reactants $LiBH_4$, $Er(BH_4)_3$ and LiH, are observed after ball milling. In addition, ErH_2 is formed in minor amounts, showing that a reaction has already started during the milling process. The products after desorption at 400 °C and 5–10 bar H_2 are mainly ErB_4 and several Er-hydrides. Cubic (c-) ErH_3 (*Fm*-3*m*) is the main phase, but small amounts of ErH_2, ErH and trigonal (t-) ErH_3 (*P*-3*c*1) are also present. As suggested above, ErH_3 appeared during cooling under hydrogen pressure. Minor Bragg peaks corresponding to ErB_{12} are detected as well. Reabsorption at 340 °C under 100 bar H_2 for 12 h led to the complete consumption of the Er borides. Trivalent Er-hydride was found after reabsorption in both the cubic and trigonal modifications.

Interestingly, the Bragg peaks of ErB_4 show less intensity in the ex situ PXD pattern of desorbed S1 in Figure 2b than in desorbed S2, although the conditions were the same. This observation let us to a hypothesis that the excess of $LiBH_4$ somehow increases the crystallinity of the material. This is supported by the observations in another recently published study, where the decomposition of pure $Er(BH_4)_3$ resulted in a completely amorphous material [36]. The crystallinity was improved by addition of LiH and by reabsorption. The products were ErH_3 and $LiBH_4$, and the final material was crystalline. Whether this observation is caused by amorphous Er–B–H species, which simply decrease when $LiBH_4$ is formed, or if the process is triggered directly by $LiBH_4/ErH_3$ formation, cannot be concluded.

TG-DSC data of S2, stored for three months in a glove box, is presented in Figure 3b. TG data show a mass loss of 3.9 wt % up to 400 °C, and DSC data show three endothermic events, two sharp and one broad. The two sharp events are the phase transition and melting of $LiBH_4$ occurring at 111 and 271 °C, respectively. These events are not related to any mass loss in the TG data. The third endothermic peak is broad, and therefore probably a superposition of the decomposition of $Er(BH_4)_3$ and $LiBH_4$ with peak temperatures at 336 and 391 °C, respectively. Figure 3bii shows H_2 (m/z = 2) desorption between 275 and 400 °C. Minor amounts of B_2H_6 (m/z = 26) are also seen in Figure 3bi, as well as $S(CH_3)_2$ (m/z = 62) between 75 and 125 °C.

Figure 4a shows in situ SR-PXD desorption data of S2, which was stored for nine months in a glove box. The RT data show significant Bragg peaks from ErH_2. Compared to the rather minor peaks of ErH_2 directly after ball milling in Figure 3a, it becomes clear that ErH_2 is formed during the storage in Ar. This observation suggests that the reaction in Equation (1) even occurs at ambient temperature for S2. Equation (1) is an intermediate reaction, showing the formation of $LiBH_4$, initiated during the milling of $Er(BH_4)_3$ and LiH, as well as the formation of ErH_2. Bragg peaks of the other phases appear for the as-milled S2 (Figure 3a) at RT. The atomic positions for Er in $Er(BH_4)_3$ were refined (Figure S3 and Table S1) and are within the standard deviations of those reported for Y in $Y(BH_4)_3$ [5]. The in situ SR-PXD desorption starts with a heating ramp from RT to 400 °C with a heating rate of 5 °C·min^{-1} and a 30-min isotherm at 400 °C. The gap in the data is due to a lost connection to the detector for 15 min in the temperature interval of 30–80 °C. The phase transition of $LiBH_4$ occurs at 100 °C. The Bragg peaks of $Er(BH_4)_3$ decrease and are gone at 195 °C, which is 55 °C lower compared to the in situ SR-PXD desorption data of S1. In any case, these observations are in agreement with earlier reports, where the halide free yttrium borohydride turns into "an X-ray amorphous solid" without melting at ~200 °C [35]. Therefore, we assume an amorphisation, as all Bragg peaks of $Er(BH_4)_3$ disappear and the DSC data indicate no melting. The amorphisation temperatures in S1 and S2 are, however, 50–100 °C lower than the reported amorphisation temperature of pure $Er(BH_4)_3$ [36]. The melting of $LiBH_4$ can be observed by the in situ SR-PXD data at 295 °C. The hydrogenation of the bivalent to trivalent erbium hydride occurs simultaneously, which is evident from a shift to lower 2θ angles for the Er hydride peaks (Figure 4a and Figure S1) and in good agreement with the in situ SR-PXD desorption data of S1. The Bragg peaks of ErH_3 increase in intensity until the heating is stopped after 30 min at 400 °C, concluding that the timeframe of the in situ SR-PXD desorption measurement for S2 does not allow for the formation of ErB_4, which is the suggested desorption product, see Equation (2).

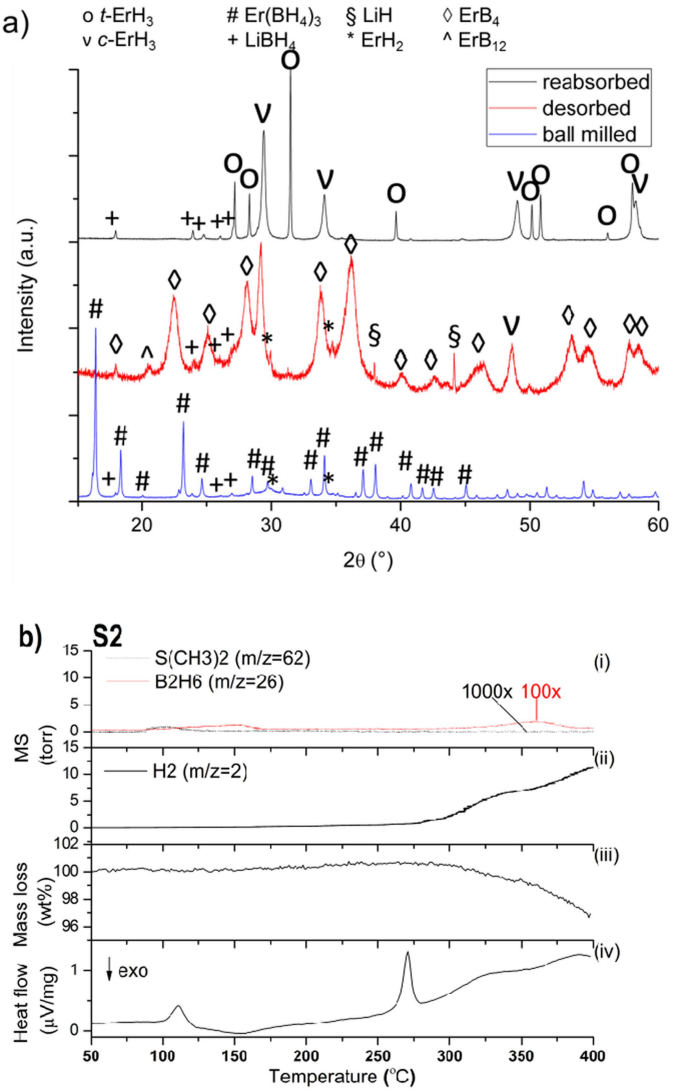

Figure 3. (**a**) Ex situ PXD data of S2 at RT showing one absorption-desorption cycle with ball milled (bottom), desorbed (middle), and reabsorbed (top) composite. λ = 1.54056 Å; (**b**) MS-TG-DSC of ball milled S2 from RT to 400 °C (heating rate 5 °C·min^{-1}) showing: (i) release of $S(CH_3)_2$ and B_2H_6; (ii) H_2; (iii) TG data; and (iv) DSC data.

The starting point of the in situ SR-PXD reabsorption is the ex-situ desorbed S2, see Figure 3a (middle, red curve). The in situ SR-PXD reabsorption of desorbed S2 was performed with a heating ramp of 5 °C·min^{-1} from RT to 340 °C under 93 bar H_2. From RT to 261 °C, the intensities of all phases appear constant. The connection to the detector was lost at 261 °C for 1 h until 42 min into the isothermal regime at 340 °C. During the connection loss, the Bragg peaks of c-ErH_3 increase moderately, while those of ErB_4 decrease slightly. This trend continues during the additional 2-h isotherm shown in Figure 4b. The minor changes in intensity indicate that it is again not possible to follow a complete hydrogenation during the timeframe of the in situ measurement.

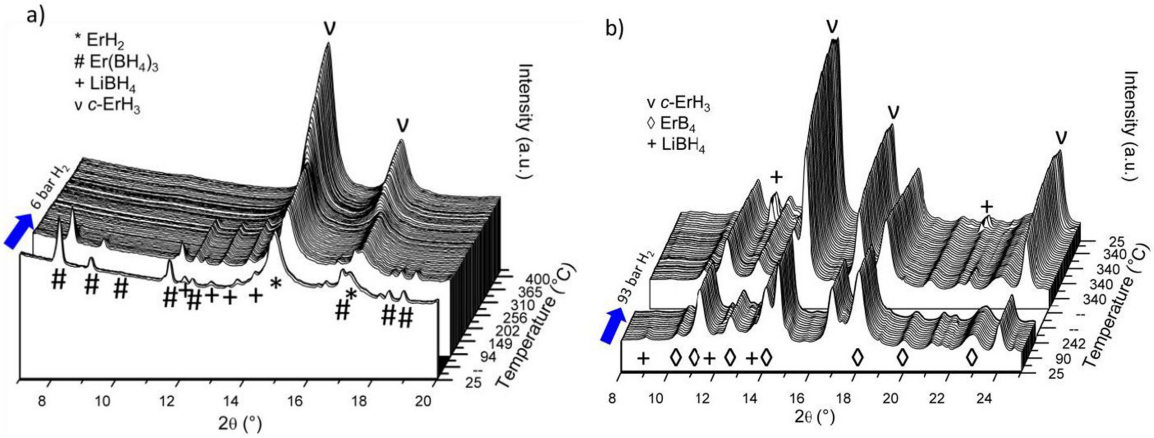

Figure 4. In situ SR-PXD data showing (**a**) desorption of S2 during heating from RT to 400 °C (5 °C·min^{-1}) under 6 bar H_2. A detector connection loss is the reason for the gaps in intensity (heating continued). λ = 0.77787 Å; (**b**) reabsorption of Sieverts apparatus desorbed S2 during heating from RT to 340 °C (5 °C·min^{-1}) under 93 bar H_2 followed by a 2-h isotherm, and cooling to RT. λ = 0.77787 Å.

Three desorption-absorption cycles were measured for S2 in a Sieverts-type apparatus. The volumetric desorption data after 5 h at 400 °C and 5–10 bar H_2 is illustrated in Figure 5. The first, second and third desorption show a hydrogen release of 4.2 wt %, 3.7 wt % and 3.5 wt %, respectively. During the first desorption of S2, $Er(BH_4)_3$ is decomposed to Er-hydride according to the ex situ PXD data, which resulted in a slower hydrogen release at the beginning of the first desorption (black curve in Figure 5). As $Er(BH_4)_3$ is not formed on rehydrogenation, this step is not repeated after the first desorption, thus resulting in a faster desorption for the second/third reabsorption.

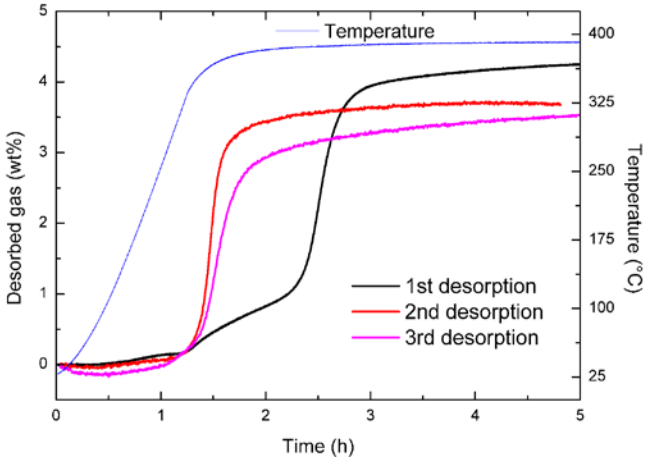

Figure 5. Hydrogen release in the first three desorption during cycling of S2 in a Sieverts-type apparatus. The hydrogen pressure is 5–10 bar.

The TG-DSC data of S2 after the first reabsorption is shown in Figure 6. The DSC signal is similar to the ball milled sample in Figure 3b. The phase transition of $LiBH_4$ shifts to a slightly lower temperature, 103 °C (111 °C for ball milled S2). The melting of $LiBH_4$ still occurs at 270 °C. The third minor endothermic peak at 322 °C in Figure 6 cannot be explained. Although the set temperature for the isotherm is 400 °C, the fourth peak was observed at a peak temperature of 403 °C (due to a slight temperature overshoot) in Figure 6. It is suggested to be the decomposition of $LiBH_4$, and hence slightly higher than for S2 after ball milling. The mass loss starts simultaneously with the fourth endothermic DSC event, also suggesting the decomposition of $LiBH_4$. The fifth peak in the isothermal

regime after 7 min at 400 °C is suggested to be the reduction of ErH_3 to ErH_2 as the mass loss continues through this event (Figure S2). The TG data in Figure 6 show a mass loss of 4.5 wt % for reabsorbed S2. Although it was reported that hydrogen pressure has a beneficial effect on desorption behavior, the TG and Sieverts data for the reabsorbed S2 show a weight loss of 4.5 and 3.7 wt %, respectively. The total hydrogen content of S2 is 9.0 wt %, but only 6.0 wt % can be obtained when forming LiH, meaning that our TG data shows a hydrogen uptake of 75%, compared to the nominal maximum value.

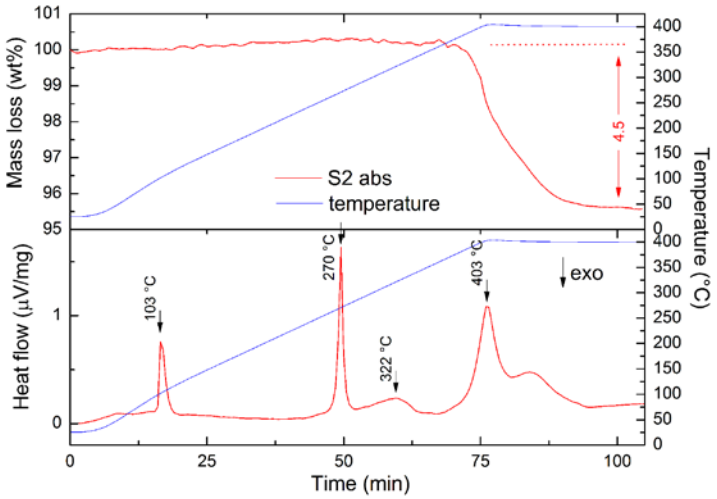

Figure 6. TG (top) and DSC (bottom) data of S2 after the first reabsorption. The *x*-axis is in time (min) as the measurement proceeds isothermally for 30 min after the heating ramp. Temperature (°C) is shown on the *y*-axis to the right.

To summarize, we observe from the PXD and SR-PXD data an increasing amount of ErB_4 during thermal decomposition and an increasing amount of $ErH_{2+\delta}$ during reabsorption for S2. This is in good agreement with the following reaction pathway, with an assumed start of decomposition similar to reaction products in Equation (1)

$$ErH_3(s) + 4LiBH_4(s) \leftrightarrow ErB_4(s) + 4LiH(s) + 7.5H_2(g) \quad (4)$$

The theoretical storage capacity of Equation (4) of 5.1 wt % H was not achieved, which is possibly caused by the uncompleted decomposition reactions, as residuals of ErH_3 have been found in decomposed samples.

The comparison of S2 to the recently investigated $6LiBH_4 + ErCl_3 + 3LiH$ composite by Frommen et al. [27] shows that the two systems behave very similar with respect to rehydrogenation. During the first reabsorption, 80% to 85% of the original hydrogen content could be reabsorbed for both systems at similar conditions. The weight loss for our system shows 4.5 wt % after one desorption-absorption cycle while 2.4 wt % was reported for the other composite [27], meaning that the absorption in our composite has almost double the hydrogen capacity after the first cycle.

There are some differences in the hydrogenation products. In our halide-free S2 composite, c-ErH_3 and t-ErH_3 are both formed during rehydrogenation with 27.4(2) wt % and 14.4(1) wt %, respectively. $LiBH_4$ is the major reabsorption product with refined 58.1(2) wt %, suggesting, as reported recently, that LiH plays a crucial role in the formation of new $LiBH_4$ at the employed conditions [36]. In Reference [27] only c-ErH_3 was observed after rehydrogenation, but no t-ErH_3, similar to our absorbed S1 sample.

2.3. Li-Ion Conductivity

The Li-ion conductivity of absorbed S1 was measured with alternating current (AC) impedance spectroscopy from RT to 140 °C (Figure 7). Further details to the experimental setup are given in

Reference [37] and the references therein. The measurement was motivated by the hypothesis that the high temperature phase of $LiBH_4$ was stabilized in the composite, thus shifting the phase transition to lower temperatures. Evidently, the absorbed S1 showed an endothermic DSC event as low as 90 °C, which we first considered to be the phase transition in $LiBH_4$ (see DSC data, red curve in Figure 2a).

Figure 7 shows the Li^+ ionic conductivity for absorbed S1, and the values are systematically lower than for pure $LiBH_4$ as expected, since $LiBH_4$ only makes up 21 wt % in the present sample (The low conductivity values for the samples can be explained by minor amounts of $LiBH_4$ after rehydrogenation. For absorbed S1 the content is approx. 2.5 molar equivalent of $LiBH_4$ corresponding to 21 wt %. This value was calculated from the mass loss shown by TG data of absorbed S1). However, upon heating above 110 °C, the conductivities reach about four orders of magnitude higher than the RT modification, which is in good agreement with the conductivity enhancement in pure $LiBH_4$ [38]. The conductivity in absorbed S1 (Figure 7) shows a slightly steeper slope than pure $LiBH_4$ [38], which manifested in the absence of the "conductivity jump" in our data. We first suggested that this observation was caused by the initial ball milling of S1. In a recent publication, it was shown that ball milled $LiBH_4$-LiI samples have a higher conductivity before annealing caused by the formation of a "defect rich microstructure," which influences the conductivity positively [39]. However, the sample chosen for impedance spectroscopy was heated to 400 °C during the first decomposition and then reabsorbed at 340 °C. This heat treatment should heal all defects and disregard their influence [39]. In summary, the high temperature phase transition is observed at 110 °C, which is in agreement with pure $LiBH_4$ [38,40]. From the Li-ion conductivity measurements, the DSC event at 90 °C for absorbed S1 cannot be explained by the high temperature phase transition of $LiBH_4$.

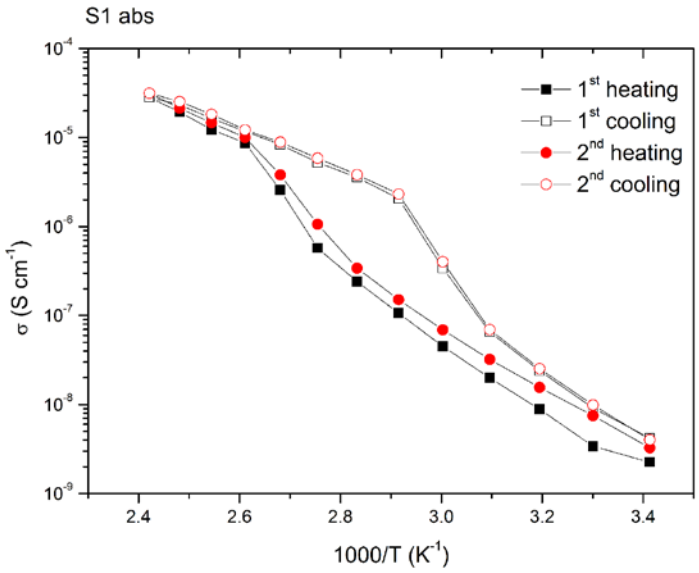

Figure 7. Li-ion conductivity measured by AC impedance spectroscopy for S1 abs. Conductivity was measured every 10 °C from RT to 140 °C and back down to RT. See text for further discussion.

However, a rather wide hysteresis is observed in Figure 7, which is in the range of 40–60 K. That is in strong contrast to the hysteresis of pure and ball milled $LiBH_4$, which is only 4 K [41], but rather close to the $LiBH_4$-LiCl system in which the hysteresis is about 20–40 K [40]. The presence of lithium halides can be ruled out, as it would significantly lower the phase transition temperature [40]. It has been observed [42] that nanoconfined $LiBH_4$ in mesoporous silica scaffolds shows a remarkable Li-conductivity in the temperature range of RT-140 °C. According to Blanchard et al. [42], the high conductivity is a consequence of two different fractions of $LiBH_4$, a bulk $LiBH_4$ fraction and a thin (1.0 nm) interfacial layer of $LiBH_4$. Assuming a morphological change in the grain size and in the inter-grains arrangement, it could be assumed that the formation of the abovementioned layer between

$LiBH_4$ and ErH_3 after several cycles of hydrogenation has happened. This can explain the inertia of the system to undergo the transition to the RT phase. The ionic conductivity contribution of this layer is dominant with respect to the bulk $LiBH_4$, however, it is not visible by diffraction due to its nanoscopic nature. This effect of nanoconfined $LiBH_4$ could explain the rather low endothermic DSC event, which were discussed above, as similar events were also reported in Reference [42].

SEM images (see Figures S4–S6) were collected, but their resolution is not sufficient to observe a 1.0-nm thin interfacial layer. Further measurements with TEM are necessary to conclude with certainty that an interfacial layer of $LiBH_4$ has formed. Due to the paramagnetic properties of erbium, it was not possible to conduct NMR.

3. Materials and Methods

$ErCl_3$ (99.9%), $LiBH_4$ (>95%), LiH (>95%) and dimethyl sulfide ($S(CH_3)_2$, anhydrous, 99.9%) were purchased from Sigma Aldrich, St. Louis, MO, USA and used as received.

The synthesis of $Er(BH_4)_3$ has been described in Reference [36]. The composite mixtures were ball milled using a Fritsch Pulverisette 6 planetary mill (Fritsch, Idar-Oberstein, Germany) employing an 80-mL tungsten carbide-coated steel vial and balls. A ball to powder ration of 40:1 was used. All sample descriptions of the composite mixtures are given in Table 1, including their composition and synthesis method as well as refined lattice parameters and phase fractions obtained by Rietveld refinements.

The samples were stored and handled in an MBraun glove box (MBraun Inertgas-Systeme GmBH, Garching, Germany) fitted with a recirculation system and oxygen/humidity sensors with H_2O/O_2 levels below 1 ppm. All procedures outside of the glove box were performed using in vacuo or Schlenk line techniques under a purified Ar atmosphere. An in-house manufactured Sieverts-type apparatus [43] was used for hydrogen desorption–absorption cycling experiments. Desorption was performed using a temperature ramp of 5 °C·min^{-1} from room temperature to 400 °C under 3 bar H_2, followed by a 12 h isothermal step. Absorption was conducted for 12 h at 340 °C and 100 bar H_2.

Powder X-ray diffraction (PXD) data were collected using a Rigaku SmartLab diffractometer (Rigaku, Tokyo, Japan). The samples were measured within rotating glass capillaries, with an inner diameter of 0.5 mm and sealed with silicone grease. All measurements were completed in Debye-Scherrer geometry using Cu$K\alpha$ radiation with λ = 1.54056 Å, over the scattering angles $2\theta = 10°–70°$.

In situ synchrotron radiation powder X-ray diffraction (SR-PXD) was executed at Swiss Norwegian Beam Lines, BM01 [44], at the European Synchrotron Radiation Facility (ESRF), Grenoble, France. The cycling experiments were conducted using a heating/cooling rate of 5 °C·min^{-1} with a typical H_2 pressure of ~100 bar for absorption and ~3 bar for desorption. Hydrogen pressure was employed for all volumetric and in situ SR-PXD experiments, as similar conditions were reported to increase gas desorption compared to desorption under vacuum [17,27,45]. Data were collected using a Pilatus 2 M detector (DECTRIS Ltd., Baden-Daettwil, Switzerland) and a sample-to-detector distance of 146 mm at wavelengths of 0.77787 Å. Wavelength and sample-to-detector distance were calibrated from an NIST LaB_6 standard. Exposure time was set to 30 s, giving a temperature resolution of 2.5 K/pattern. The sample was contained in a single-crystal sapphire tube (inner diameter 0.8 mm) connected to the cell with Vespel ferrules and Swagelok fittings. Hydrogen was introduced and removed from the cell with an in-house built computer-controlled gas rig. The cell was rotated by 10° to improve powder averaging during each exposure. The single-crystal reflections from the sapphire tubes were masked out manually in Fit2D [46]. Rietveld refinements were performed with GSAS and Expgui software [47,48]. Thompson-Cox-Hastings pseudo-Voigt functions with three Gaussian and one Lorentzian parameter were used to model the Bragg peak profiles [49]. The background was fitted with a shifted Chebyshev polynomial with up to 36 terms. The atomic positions for the $Er(BH_4)_3$ were taken from $Y(BH_4)_3$ [5] and refined with the data shown in Figure S3 at room temperature. BH_4 units were treated as rigid bodies with B–H distances of 1.13 Å.

Simultaneous thermogravimetric and differential scanning calorimetry (TG-DSC) experiments were carried out with a Netzsch STA 449 F3 Jupiter instrument (Netzsch, Bavaria, Germany). In some measurements, mass spectrometry (MS) was performed simultaneously by connecting a Hiden Analytical HPR-20 QMS (Hiden, Warrington, UK) to the TG-DSC. The samples were loaded in aluminum crucibles (~5–10 mg) and were heated up to 400–500 °C with a heating rate of 5 °C·min^{-1}. An argon flow of 70 mL·min^{-1} was used as a protection gas and purge gas. All given temperatures are peak temperatures, unless stated otherwise.

Li-ion conductivity was measured by impedance spectroscopy, employing an HP 4192A FL impedance analyzer (Keysight Technologies, Santa Rosa, CA, USA). The frequency range was 5 Hz to 10 MHz with a signal amplitude of 60 mV. The temperature was varied by 10 °C for each measurement from RT to 140 °C, and back to RT. Three sets were performed for each measurement in order to improve reproducibility. A 3-ton mechanical axial press was used for pressing pellets with a typical diameter of 6.35 mm and a thickness of 0.5–1.0 mm. The samples were placed in a BDS 1200 Novocontrol sample cell (Novocontrol Technologies GmbH Co. KG, Montabaur, Germany) under an argon atmosphere between two gold ion-blocking electrodes. A single parallel resistor(R)-constant phase element (CPE) was used as an equivalent circuit at low temperatures, where the noise is higher. At higher temperatures, additional effects were taken into account, such as the polarization of the electrode interfaces (modeled with a single CPE) and, eventually, a second R-CPE parallel circuit due to grain boundary contributions. A Hitachi S-4800 Scanning electron microscope (SEM) (Hitachi, Tokyo, Japan) equipped with a Noran System Six energy dispersive spectrometer (EDS) was employed for investigating the absorbed S1 after the conductivity measurements.

4. Conclusions

This work characterized two new composite materials consisting of $Er(BH_4)_3$, $LiBH_4$ and/or LiH. The composites react during ball milling, storage as well as decomposition in a two-step reaction where Er-hydrides and $LiBH_4$ are formed in the first step. ErB_4 is formed in a second step during thermal decomposition. The composites can be cycled between the first and second decomposition steps by applying hydrogen pressure. Volumetric measurements show a hydrogen capacity of 88% after the first cycle of the initially released hydrogen content and seem stable after the third cycle, with 95% rehydrogenation compared to the second cycle. With a weight loss of 4.5 wt % after the first desorption–absorption cycle, the hydrogen capacity had almost doubled compared to earlier investigated systems, which included LiCl.

Li-ion conductivity measurements of absorbed $Er(BH_4)_3$ + 6LiH showed an exceptional high hysteresis of 40–60 K for the transition between the high and low temperature phases of $LiBH_4$, which may be a good starting point to investigate further, for all solid state Li-ion batteries.

Supplementary Materials: The following are available online at www.mdpi.com/2304-6740/5/2/31/s1. Figure S1: SR-PXD data of thermal desorption of S1 and S2, Figure S2: TG-DSC data of pure ErH_3 between 25 and 1000 °C. Figure S3: SR-PXD Rietveld refinement and difference plot of S2, Figures S4–S6: SEM image of the absorbed S1. Figure S7: SR-PXD Rietveld refinement and difference plot of S1, Figure S8: PXD Rietveld refinement and difference plot of S2, Table S1: Atomic positions and displacement factor refined for Er and B in $Er(BH_4)_3$.

Acknowledgments: The research leading to these results has received funding from the People Program (Marie Curie Actions) of the European Union's Seventh Framework Program FP7/2007–2013/ under REA grant agreement n° 607040 (Marie Curie ITN ECOSTORE) and is thankfully acknowledged. The authors acknowledge the skillful assistance from the staff of the Swiss-Norwegian Beamline, at the European Synchrotron Radiation Facility, Grenoble, France.

Author Contributions: Michael Heere was involved in all stages of the reported work, from planning and conducting of most experiments to the analysis of the data. Michael Heere wrote the first draft of the manuscript, implemented feedback from the co-authors and submitted the work. Michael Heere will include the requests of the reviewers and accompany the whole submission process to its completion. Seyed Hosein Payandeh GharibDoust was involved in all stages of the reported work, from planning and helping with experiments to the analysis of the data. He contributed with the synthesis method and helped in various experiments started from MS-TG-DSC, PXD, SR-PXD including the help with analysis of the data. Magnus H. Sørby and Christoph Frommen acted as co-supervisors and main co-reader/writer. They helped with Rietveld refinement and with data anaylsis from

synchrotron radiation powder X-ray diffraction experiments. Matteo Brighi and Radovan Černý conducted the impedance spectroscopy experiments, analysed the data and added valuable sections in the discussion of the results. Torben R. Jensen and Bjørn C. Hauback acted as main supervisor for this work. They contributed to initiate the work, followed up the experiments in Aarhus and Kjeller, respectively, and helped with the preparation of the manuscript.

Conflicts of Interest: The authors declare no conflict of interest.

References

1. Züttel, A.; Rentsch, S.; Fischer, P.; Wenger, P.; Sudan, P.; Mauron, P.H.; Emmenegger, C.H. Hydrogen storage properties of $LiBH_4$. *J. Alloys Compd.* **2003**, *356–357*, 515–520. [CrossRef]
2. Züttel, A.; Borgschulte, A.; Orimo, S.I. Tetrahydroborates as new hydrogen storage materials. *Scr. Mater.* **2007**, *56*, 823–828. [CrossRef]
3. Mauron, P.; Buchter, F.; Friedrichs, O.; Remhof, A.; Bielmann, M.; Zwicky, C.N.; Züttel, A. Stability and Reversibility of $LiBH_4$. *J. Phys. Chem. B* **2008**, *112*, 906–910. [CrossRef] [PubMed]
4. Pitt, M.P.; Paskevicius, M.; Brown, D.H.; Sheppard, D.A.; Buckley, C.E. Thermal Stability of $Li_2B_{12}H_{12}$ and its Role in the Decomposition of $LiBH_4$. *J. Am. Chem. Soc.* **2013**, *135*, 6930–6941. [CrossRef] [PubMed]
5. Sato, T.; Miwa, K.; Nakamori, Y.; Ohoyama, K.; Li, H.W.; Noritake, T.; Aoki, M.; Towata, S.I.; Orimo, S.I. Experimental and computational studies on solvent-free rare-earth metal borohydrides $R(BH_4)_3$ (R = Y, Dy, and Gd). *Phys. Rev. B* **2008**, *77*, 104–114. [CrossRef]
6. Olsen, J.E.; Frommen, C.; Sørby, M.H.; Hauback, B.C. Crystal structures and properties of solvent-free $LiYb(BH_4)_{4-x}Cl_x$, $Yb(BH_4)_3$ and $Yb(BH_4)_{2-x}Cl_x$. *RSC Adv.* **2013**, *3*, 10764–10774. [CrossRef]
7. Jaroń, T.; Grochala, W. $Y(BH_4)_3$—An old-new ternary hydrogen store aka learning from a multitude of failures. *Dalton Trans.* **2010**, *39*, 160–166. [CrossRef] [PubMed]
8. Frommen, C.; Aliouane, N.; Deledda, S.; Fonneløp, J.E.; Grove, H.; Lieutenant, K.; Llamas-Jansa, I.; Sartori, S.; Sørby, M.H.; Hauback, B.C. Crystal structure, polymorphism, and thermal properties of yttrium borohydride $Y(BH_4)_3$. *J. Alloys Compd.* **2010**, *496*, 710–716. [CrossRef]
9. Frommen, C.; Sørby, M.H.; Ravindran, P.; Vajeeston, P.; Fjellvåg, H.; Hauback, B.C. Synthesis, crystal structure, and thermal properties of the first mixed-metal and anion-substituted rare earth borohydride $LiCe(BH_4)_3Cl$. *J. Phys. Chem. C* **2011**, *115*, 23591–23602. [CrossRef]
10. Ravnsbæk, D.B.; Filinchuk, Y.; Černý, R.; Ley, M.B.; Haase, D.; Jakobsen, H.J.; Skibsted, J.; Jensen, T.R. Thermal polymorphism and decomposition of $Y(BH_4)_3$. *Inorg. Chem.* **2010**, *49*, 3801–3809. [CrossRef] [PubMed]
11. Ley, M.B.; Jepsen, L.H.; Lee, Y.S.; Cho, Y.W.; von Colbe, J.M.B.; Dornheim, M.; Rokni, M.; Jensen, J.O.; Sloth, M.; Filinchuk, Y. Complex hydrides for hydrogen storage—New perspectives. *Mater. Today* **2014**, *17*, 122–128. [CrossRef]
12. Yan, Y.; Li, H.W.; Sato, T.; Umeda, N.; Miwa, K.; Towata, S.; Orimo, S. Dehydriding and rehydriding Properties of yttrium borohydride $Y(BH_4)_3$ prepared by liquid-phase synthesis. *Int. J. Hydrogen Energy* **2009**, *34*, 5732–5736. [CrossRef]
13. Jaron, T.; Kozminski, W.; Grochala, W. Phase transition induced improvement in H_2 desorption kinetics: The case of the high-temperature form of $Y(BH_4)_3$. *Phys. Chem. Chem. Phys.* **2011**, *13*, 8847–8851. [CrossRef] [PubMed]
14. Gennari, F.C.; Esquivel, M.R. Synthesis and dehydriding process of crystalline $Ce(BH_4)_3$. *J. Alloys Compd.* **2009**, *485*, L47–L51. [CrossRef]
15. Li, H.W.; Yan, Y.; Orimo, S.I.; Züttel, A.; Jensen, C.M. Recent Progress in Metal Borohydrides for Hydrogen Storage. *Energies* **2011**, *4*, 185–214. [CrossRef]
16. Zhang, B.J.; Liu, B.H.; Li, Z.P. Destabilization of $LiBH_4$ by (Ce, La)(Cl, F)$_3$ for hydrogen storage. *J. Alloys Compd.* **2011**, *509*, 751–757. [CrossRef]
17. Gennari, F.; Albanesi, L.F.; Puszkiel, J.; Larochette, P.A. Reversible hydrogen storage from $6LiBH_4$–MCl_3 (M = Ce, Gd) composites by in-situ formation of MH_2. *Int. J. Hydrogen Energy* **2011**, *36*, 563–570. [CrossRef]
18. Paskevicius, M.; Jepsen, L.H.; Schouwink, P.; Černý, R.; Ravnsbæk, D.B.; Filinchuk, Y.; Dornheim, M.; Besenbacher, F.; Jensen, T.R. Metal borohydrides and derivatives—Synthesis, structure and properties. *Chem. Soc. Rev.* **2017**, *46*, 1565–1634. [CrossRef] [PubMed]

19. Callini, E.; Atakli, Z.Ö.K.; Hauback, B.C.; Orimo, S.; Jensen, C.; Dornheim, M.; Grant, D.; Cho, Y.W.; Chen, P.; Hjörvarsson, B.; et al. Complex and liquid hydrides for energy storage. *Appl. Phys. A* **2016**, *122*, 353. [CrossRef]
20. Ley, M.B.; Boulineau, S.; Janot, R.; Filinchuk, Y.; Jensen, T.R. New Li Ion Conductors and Solid State Hydrogen Storage Materials: $LiM(BH_4)_3Cl$, M = La, Gd. *J. Phys. Chem. C* **2012**, *116*, 21267–21276. [CrossRef]
21. Skripov, A.V.; Soloninin, A.V.; Ley, M.B.; Jensen, T.R.; Filinchuk, Y. Nuclear Magnetic Resonance Studies of BH_4 Reorientations and Li Diffusion in $LiLa(BH_4)_3Cl$. *J. Phys. Chem. C* **2013**, *117*, 14965–14972. [CrossRef]
22. Ley, M.B.; Ravnsbæk, D.B.; Filinchuk, Y.; Lee, Y.S.; Janot, R.l.; Cho, Y.W.; Skibsted, J.; Jensen, T.R. $LiCe(BH_4)_3Cl$, a new lithium-ion conductor and hydrogen storage material with isolated tetranuclear anionic clusters. *Chem. Mater.* **2012**, *24*, 1654–1663. [CrossRef]
23. Roedern, E.; Lee, Y.S.; Ley, M.B.; Park, K.; Cho, Y.W.; Skibsted, J.; Jensen, T.R. Solid state synthesis, structural characterization and ionic conductivity of bimetallic alkali-metal yttrium borohydrides $MY(BH_4)_4$ (M = Li and Na). *J. Mater. Chem. A* **2016**, *4*, 8793–8802. [CrossRef]
24. Marks, S.; Heck, J.G.; Habicht, M.H.; Oña-Burgos, P.; Feldmann, C.; Roesky, P.W. $[Ln(BH_4)_2(THF)_2]$(Ln = Eu, Yb)—A Highly Luminescent Material. Synthesis, Properties, Reactivity, and NMR Studies. *J. Am. Chem. Soc.* **2012**, *134*, 16983–16986. [PubMed]
25. Schouwink, P.; Ley, M.B.; Tissot, A.; Hagemann, H.; Jensen, T.R.; Smrčok, Ľ.; Černý, R. Structure and properties of complex hydride perovskite materials. *Nat. Commun.* **2014**, *5*, 5706. [CrossRef] [PubMed]
26. Schouwink, P.; Didelot, E.; Lee, Y.S.; Mazet, T.; Černý, R. Structural and magnetocaloric properties of novel gadolinium borohydrides. *J. Alloys Compd.* **2016**, *664*, 378–384. [CrossRef]
27. Frommen, C.; Heere, M.; Riktor, M.D.; Sørby, M.H.; Hauback, B.C. Hydrogen storage properties of rare earth (RE) borohydrides (RE = La, Er) in composite mixtures with $LiBH_4$ and LiH. *J. Alloys Compd.* **2015**, *645*, S155–S159. [CrossRef]
28. James, B.; Wallbridge, M. Metal tetrahydroborates. *Prog. Inorg. Chem.* **1970**, *11*, 99–231.
29. Visseaux, M.; Bonnet, F. Borohydride complexes of rare earths, and their applications in various organic transformations. *Coord. Chem. Rev.* **2011**, *255*, 374–420. [CrossRef]
30. Yang, C.H.; Tsai, W.T.; Chang, J.K. Hydrogen desorption behavior of vanadium borohydride synthesized by modified mechano-chemical process. *Int. J. Hydrogen Energy* **2011**, *36*, 4993–4999. [CrossRef]
31. Korablov, D.; Ravnsbæk, D.B.; Ban, V.; Filinchuk, Y.; Besenbacher, F.; Jensen, T.R. Investigation of MBH_4–VCl_2, M = Li, Na or K. *Int. J. Hydrogen Energy* **2013**, *38*, 8376–8383. [CrossRef]
32. Gennari, F.C. Mechanochemical synthesis of erbium borohydride: Polymorphism, thermal decomposition and hydrogen storage. *J. Alloys Compd.* **2013**, *581*, 192–195. [CrossRef]
33. Olsen, J.E.; Frommen, C.; Jensen, T.R.; Riktor, M.D.; Sørby, M.H.; Hauback, B.C. Structure and thermal properties of composites with RE-borohydrides (RE = La, Ce, Pr, Nd, Sm, Eu, Gd, Tb, Er, Yb or Lu) and $LiBH_4$. *RSC Adv.* **2014**, *4*, 1570–1582. [CrossRef]
34. Hagemann, H.; Černý, R. Synthetic approaches to inorganic borohydrides. *Dalton Trans.* **2010**, *39*, 6006–6012. [CrossRef] [PubMed]
35. Ley, M.B.; Paskevicius, M.; Schouwink, P.; Richter, B.; Sheppard, D.A.; Buckley, C.E.; Jensen, T.R. Novel solvates $M(BH_4)_3S(CH_3)_2$ and properties of halide-free $M(BH_4)_3$ (M = Y or Gd). *Dalton Trans.* **2014**, *43*, 13333–13342. [CrossRef] [PubMed]
36. Heere, M.; Payandeh GharibDoust, S.H.; Frommen, C.; Humphries, T.D.; Ley, M.B.; Sørby, M.H.; Jensen, T.R.; Hauback, B.C. The influence of LiH on the rehydrogenation behavior of halide free rare earth (RE) borohydrides (RE = Pr, Er). *Phys. Chem. Chem. Phys.* **2016**, *18*, 24387–24395. [CrossRef] [PubMed]
37. Brighi, M.; Schouwink, P.; Sadikin, Y.; Černý, R. Fast ion conduction in garnet-type metal borohydrides $Li_3K_3Ce_2(BH_4)_{12}$ and $Li_3K_3La_2(BH_4)_{12}$. *J. Alloys Compd.* **2016**, *662*, 388–395. [CrossRef]
38. Maekawa, H.; Matsuo, M.; Takamura, H.; Ando, M.; Noda, Y.; Karahashi, T.; Orimo, S.I. Halide-Stabilized $LiBH_4$, a Room-Temperature Lithium Fast-Ion Conductor. *J. Am. Chem. Soc.* **2009**, *131*, 894–895. [CrossRef] [PubMed]
39. Sveinbjörnsson, D.; Myrdal, J.S.G.; Blanchard, D.; Bentzen, J.J.; Hirata, T.; Mogensen, M.B.; Norby, P.; Orimo, S.I.; Vegge, T. Effect of Heat Treatment on the Lithium Ion Conduction of the $LiBH_4$–LiI Solid Solution. *J. Phys. Chem. C* **2013**, *117*, 3249–3257. [CrossRef]

40. Matsuo, M.; Takamura, H.; Maekawa, H.; Li, H.W.; Orimo, S.I. Stabilization of lithium superionic conduction phase and enhancement of conductivity of $LiBH_4$ by LiCl addition. *Appl. Phys. Lett.* **2009**, *94*, 084103. [CrossRef]
41. Nakamori, Y.; Orimo, S.I.; Tsutaoka, T. Dehydriding reaction of metal hydrides and alkali borohydrides enhanced by microwave irradiation. *Appl. Phys. Lett.* **2006**, *88*, 112104. [CrossRef]
42. Blanchard, D.; Nale, A.; Sveinbjörnsson, D.; Eggenhuisen, T.M.; Verkuijlen, M.H.; Vegge, T.; Kentgens, A.P.; Jongh, P.E. Nanoconfined $LiBH_4$ as a fast lithium ion conductor. *Adv. Funct. Mater.* **2015**, *25*, 184–192. [CrossRef]
43. Brinks, H.; Fossdal, A.; Bowman, R.; Hauback, B.C. Pressure–composition isotherms of $TbNiAlH_x$. *J. Alloys Compd.* **2006**, *417*, 92–95. [CrossRef]
44. Dyadkin, V.; Pattison, P.; Dmitriev, V.; Chernyshov, D. A new multipurpose diffractometer PILATUS@SNBL. *J. Synchrotron Radiat.* **2016**, *23*, 825–829. [CrossRef] [PubMed]
45. Shim, J.H.; Lim, J.H.; Rather, S.; Lee, Y.S.; Reed, D.; Kim, Y.; Book, D.; Cho, Y.W. Effect of Hydrogen Back Pressure on Dehydrogenation Behavior of $LiBH_4$-Based Reactive Hydride Composites. *J. Phys. Chem. Lett.* **2010**, *1*, 59–63. [CrossRef]
46. Hammersley, A. *FIT2D: An Introduction and Overview*; European Synchrotron Radiation Facility Internal Report ESRF97HA02T; European Synchrotron Radiation Facility: Grenoble, France, 1997.
47. Larson, A.; Von Dreele, R. *General Structure Analysis System (GSAS)*; Report LAUR 86-748; Los Alamos National Laboratory: Los Alamos, NM, USA, 2000.
48. Toby, B.H. *EXPGUI*, a graphical user interface for *GSAS*. *J. Appl. Crystallogr.* **2001**, *34*, 210–213. [CrossRef]
49. Thompson, P.; Cox, D.; Hastings, J. Rietveld refinement of Debye–Scherrer synchrotron X-ray data from Al_2O_3. *J. Appl. Crystallogr.* **1987**, *20*, 79–83. [CrossRef]